



OTC-25196

Characterization of the Slope-destabilizing Effects of Gas-charged Sediment via Seismic Surveys

Eugene Morgan, Duke University; Maarten Vanneste, NGL; Mark Vardy, University of Southampton

Copyright 2014, Offshore Technology Conference

This paper was prepared for presentation at the Offshore Technology Conference held in Houston, Texas, USA, 5–8 May 2014.

This paper was selected for presentation by an OTC program committee following review of information contained in an abstract submitted by the author(s). Contents of the paper have not been reviewed by the Offshore Technology Conference and are subject to correction by the author(s). The material does not necessarily reflect any position of the Offshore Technology Conference, its officers, or members. Electronic reproduction, distribution, or storage of any part of this paper without the written consent of the Offshore Technology Conference is prohibited. Permission to reproduce in print is restricted to an abstract of not more than 300 words; illustrations may not be copied. The abstract must contain conspicuous acknowledgment of OTC copyright.

Abstract

Finneid fjord, Norway has a history of submarine slope failure and hosts areas of buried, gas-charged sediment. Using shipboard seismic survey data from Finneid fjord, we illustrate how novel seismic data processing techniques can yield estimates of geotechnical properties of this gas-charged sediment: gas saturation (concentration) and excess pore pressure as well as their uncertainty. This data processing involves two steps: 1) estimate the amount of seismic attenuation that a gas-bearing layer creates, and 2) fit a wave attenuation model to the observed attenuation. We accomplish the first step using a wavelet-based spectral ratio approach, and find the seismic quality factor (inversely related to attenuation) from the change in amplitude spectra across the gas layer. The novelty of this paper really comes in the second step, where we create a Bayesian hierarchical model that combines a wave attenuation model with a spatial random (Gaussian) process model. The advantage of this combination is that our estimates of the gas properties not only must conform to the observations of attenuation (quality factor), but must also smoothly vary over space, as one would expect of any natural process. Ultimately, we end up with posterior distributions of gas properties at points throughout our gas-bearing layer, which give us estimates of parameter values and a sense of uncertainty about these estimates. We find good performance and agreeable values for gas saturation, but the model shows weak sensitivity to pressure, leaving large uncertainty in any excess pore pressure estimates.

Implications for slope stability at Finneid fjord are discussed.

Introduction

Estimating the distribution of free gas in the subsurface has traditionally been a problem important for resource exploration. In Finneid fjord, Norway, which hosts both shallow deposits of gas-charged sediment and a history of landslides, determining the properties of this subsurface gas is necessary for characterizing its role in slope stability. Finneid fjord has been the subject of recent, active field investigation, partially for these reasons (Vanneste et al. (2013), Vardy et al. (2012)). Theoretically, the accumulation of subsurface gas can lead to excess pore pressures, which would in turn weaken sediments. The presence of the free gas can clearly be seen in seismic images of the sub-seabed sediments in the fjord; at the top of the gas-bearing layer one sees the distinctive negative polarity reflection, and below this, “gas-blanking” or muting of the signal, as is common with gas deposits. The distinctive presence of gas in seismic data, the wide spatial coverage of seismic surveys, and relative ease of collecting seismic data (versus invasive, in situ devices or soil sampling) all make shipboard seismics an attractive means of investigating natural gas deposits. The goal of this paper is to illustrate a method for estimating the distribution of gas saturation and pressure from seismic profile data.

A common approach to characterizing gas with seismics is to use velocity, but seismic velocities do not show great sensitivity to hydraulic properties. For example, Bunz et al. (2005) estimate free gas concentration with P- and S-wave velocity analysis from ocean-bottom seismometer data. Without relying on in situ measurements, Ecker et al. (2000) invert a rock-physics model to estimate gas hydrate and free gas concentrations from interval velocities obtained from AVO analysis of multichannel seismic data. However, Ecker et al. (2000) note that their saturation estimates show extreme sensitivity to their velocity-interval values, and, in a different study, Zillmer (2006) concludes that small uncertainties in seismic velocities can lead to large variances in gas saturation estimates. Furthermore, Lee and Collett (2009) examine well-log velocities for $V_p/V_s < 2$ (an indicator of gas presence), but note that this does not work well for low gas saturations.

Seismic attenuation, on the other hand, has a strong dependence on the hydraulic properties of partially saturated media, including gas saturation (White, 1975), which makes models of attenuation well suited for inverting for these hydraulic properties. In a very basic sense, the reason for this strong dependency is because a fast P-wave will convert energy to a slow

P-wave as a result of creating differential pressures between the gas and water in the pore space of a partially-saturated soil. Carcione and Picotti (2006) model this behavior at the mesoscopic scale (larger than grain size but smaller than the wavelength), which has had better success than the micro- or macroscopic scales at modeling attenuation over seismic frequencies. Morgan et al. (2012) adapt the model of Carcione and Picotti (2006) into a genetic algorithm in order to invert for gas saturation, and show that this method can estimate very low gas saturations (~0.1%). However, because of the stochastic nature of the genetic algorithm, considerable location-to-location variability may occur in the resulting gas saturation estimates.

The goal of this paper is to improve on the inversion of Morgan et al. (2012) and reduce the aforementioned variability by adding spatial dependence to the attenuation model. To do this, we will use a Bayesian hierarchical model, which also has the advantage of not just giving us point estimates at each location, but rather entire posterior distributions of each parameter in the attenuation model. Thus, we get a characterization of the uncertainty of our estimates. Many studies take Bayesian approaches to various inversion problems (e.g., Hou et al. (2006), Stenerud et al. (2008)), but we are not aware of any that apply such techniques to attenuation models as we do here.

In the following, we will first discuss the theoretical attenuation model, and throughout the paper refer to this model as a simulator (or forward model). This language will help reduce confusion when we introduce the hierarchical model later on. After the Theoretical Model section, we present the seismic data to be used for this study, and go on to talk about our procedure for measuring quality factor (related to attenuation) from the seismic data. We then discuss the Bayesian hierarchical model, followed by the results and subsequent discussion.

Theoretical Model

For our hierarchical model to work, we need a simulator that will take values of physical parameters and return the corresponding attenuation (or quality factor (Q), which is inversely proportional to attenuation). For this purpose, we adopt the P-wave attenuation model presented in Carcione and Picotti (2006), which is essentially the model of White (1975) with periodic layering. The exact equations we use to calculate Q are presented in the Appendix. Assuming that the gas inhomogeneities are arranged in a periodic fashion may not be entirely realistic, but Dutta and Seri (1979) find that White's model is not sensitive to the arrangement of gas inclusions. It is certainly possible to explore different configurations (e.g., random layering) by altering the attenuation simulator. We will note this attenuation simulator as $g(x)$, where x is a vector containing values for the 13 parameters listed in Table 1.

While the initial values of the parameters are not so important as the parameter bounds, it is worth mentioning that we start the algorithm (discussed below) under the assumption that there is no gas and no excess pore pressure. Total pore pressure P has an initial value and lower bound equal to hydrostatic pressure at the top of the gas-bearing layer. Geotechnical testing of samples from nearby in Finneidfjord yielded a porosity of 65%; we expect the conditions here to be similar, but acknowledge some uncertainty in this measurement by giving it bounds $\pm 1\%$. Other values in Table 1 are either taken from literature sources (noted with superscripts) pertaining to similar seabed sediments, or are set arbitrarily. Our determination of layer thickness is discussed in the next section.

Data and Methods

Data

The Finneidfjord data set used here consists of a grid of 2D seismic lines collected in 2006 (Figure 1). The air-gun source operated at frequencies between 40 and 500 Hz. Data were recorded in a single-channel streamer towed at near-zero offset. Besides "gas-blanking" and a high-amplitude, reverse-polarity reflection in the seismics, free gas also shows up as bubbles in X-rays of a core taken from the gas zone (hatched area in Figure 1). For this paper, we choose to focus on one seismic line (Line 08, Figure 2) going through the zone of gas-bearing sediment.

To get the best quality data for measuring attenuation, all seismic data underwent some basic processing steps to reduce noise and provide the most appropriate reflection amplitudes. We performed amplitude gain correction on all traces to correct for spherical spreading of the seismic wave with depth. Also, we corrected for multiple attenuation via f-k filtering. Band-pass filtering, with corner frequencies of 20, 40, 500, and 600 Hz, removed some high-frequency noise as well.

We select an upper portion of the free gas zone to be analyzed because free gas migrates upward, and so this upper portion will likely have the highest gas saturation (if not contain all the gas), and thus be of most interest. We use the high-amplitude, reverse-polarity reflection to guide our pick of the top of the gas layer (Figure 3a), because this represents the shallowest limit of free gas and is easily identifiable. To mitigate interference (amplitude tuning) with the top horizon and to allow enough time separation for attenuation to occur, we choose the bottom horizon to be twice the period of the lowest frequency below the top: $t_{bottom} = t_{top} - 2/f_{minimum}$, where t is the two-way travel time, and $f_{minimum} = 40$ Hz. Thus, assuming an average velocity $V_p = 1500$ m/s, our layer thickness is 37.5 m, which corresponds to one wavelength of the lowest frequency for this survey. The following analyses only pertain to this layer, and do not inform us about the properties of gas below it.

Measuring Quality Factor

First, it is important to state that we are only capable of measuring the effective (or apparent) quality factor Q_{eff} of our chosen layer. Q_{eff} is composed of the intrinsic quality factor (Q_i), which relates to material properties and fluid flow, and the scattering quality factor Q_{sc} , which relates to the geometry of reflectors and heterogeneities. Because we are interested in free gas, and because free gas primarily affects fluid flow, we wish to measure Q_i directly, but cannot. We can, however, argue that Q_{sc} has a negligible effect in our data. The bulk of the seismic energy exists below 100 Hz, and using the formula for the scattering relaxation frequency: $f_s = V_p/(2\pi h)$, with $V_p = 1500$ m/s, h has to be at least 3 m in order for f_s to fall below 100 Hz. This could result from the gas inclusions themselves being 3 m in diameter, or having a spacing of 3 m. We know from the core taken in the gas zone that neither of these are the case at Finneidfjord. Therefore, we will measure Q_{eff} (and call it Q from here forward for simplicity) and use it to reasonably approximate Q_i , but acknowledge that some error exists here. In fact this error is included in the hierarchical model below.

The spectral ratio method estimates Q by taking the ratio of the spectra from the top and bottom reflections (associated with the horizons, in this case) and fitting a curve to the natural log of this ratio, where Q is a coefficient in the curve. In terms of obtaining the amplitude spectra, Reine et al. (2009) note that using a wavelet transform reduces the sensitivity to the choice of bandwidth over which to perform the regression. We apply a continuous wavelet transform with a Morlet wavelet (with a frequency shift of 5) to each trace in the seismic profile, at both the top and bottom travel times described above. However, before applying the transform we flatten and stack each trace with the 10 neighboring traces on either side in order to increase the signal-to-noise ratio and also get more smoothly-varying Q estimates across the profile. Here we use a brute stack (boxcar weighting) but other weighting strategies could be employed instead (e.g., Gaussian weighting).

After extracting the spectra for the top and bottom horizons, we calculate Q via linear regression with frequency f using: $\ln\left(\frac{S_{bottom}(f)}{S_{top}(f)}\right) = -\frac{\pi\Delta t}{Q}f$, where Δt is the traveltimes separating the two horizons. We choose a bandwidth of 200-250 Hz over which to perform this regression, as this contains most of the seismic energy. More details on measuring quality factor can be found in Morgan et al. (2012).

Hierarchical Model

With $Q = (Q_1, \dots, Q_m)^T$ measured at m locations (traces) containing a spatial field of gas and sediment property values $x = (x_1, \dots, x_m)^T$, we can link our observed quality factors to the unknown field via $Q = g(x) + e$, where e includes measurement error of Q and model error in our simulator $g(x)$. This is an inverse problem, where we want to use the information we have in Q to infer values in the spatial parameters x , except with the hierarchical model, we will infer posterior distributions for each parameter in x , thus giving us a measure of uncertainty as well.

The posterior distribution of x given Q is proportional to the likelihood of Q given $g(x)$ times the prior distribution of x . Here we will assume that the error e is Gaussian with zero mean, so that the likelihood is $L(Q|g(x)) \propto \exp(-\frac{1}{2\sigma^2}(Q - g(x))^T(Q - g(x)))$, where σ is the standard deviation of Q . We base our prior on a Markov random field for its renowned ability to detect edges (of gas patches, for example) and encourage similarity between neighboring values. The prior takes the form $\pi(x) \propto \exp(\beta \sum_{i \sim j} u(x_i - x_j))$, where $u(\cdot)$ is the tricube function:

$$u(d) = \begin{cases} \frac{1}{s} \left(1 - \left(\frac{d}{s}\right)^3\right)^3, & \text{if } -s < d < s, \\ 0, & \text{if } |d| \geq s. \end{cases}$$

Because the sum is over all sets of adjacent traces (nearest neighbors, $i \sim j$), it is primarily the tricube function that builds spatial dependence in our model. The constants β and s control the regularity of the parameter field over space, and we found acceptable values to be 0.5 and 0.3, respectively. To measure the distance between vectors of parameter values, we use

a normalized Euclidean distance $x_i - x_j = \sqrt{\sum_{k=1}^{13} (x_{ik} - x_{jk})^2 / s_k^2}$, where s_k is the standard deviation for the k^{th} parameter.

We set these standard deviations as the differences between the lower and upper bounds in Table 1, divided by 100.

We use a Markov Chain Monte Carlo algorithm (single-site Metropolis algorithm) to compute samples from the posterior distribution above. Details on how this algorithm is formulated are given in Higdon et al. (2008), but the main features are that it loops over all m traces n times, randomly-generating a proposed x sample each iteration, and then keeping that x if its posterior density is U times greater than the previous posterior density, where U is a random value between 0 and 1. Here we use a truncated, multivariate normal distribution (with mean equal to the last accepted x , standard deviation s_k as defined above, and truncation boundaries as defined in Table 1) to randomly-generate new x samples. Ideally, the proposed sample is accepted roughly half of the time, but acceptance rates between 30-70% are typically sufficient. Here we use $n=100,000$, and, following common practice, discard the first 10,000 samples and keep only every tenth sample after that (in order to mitigate dependence between samples).

Results

Our measurements of quality factor (Q) are presented in Figure 3b. Across the gas zone, our Q values stay in the 10-60 range, which is appropriate for gas-bearing sediment. These values vary smoothly over the profile, with a slight trend towards higher Q values at the right side (larger Trace Numbers).

Figure 4 presents the posterior probability density distributions for all traces across the profile. These are presented as a raster image, where each column belongs to a separate trace and each color indicates the probability density of the gas saturation values. Thus, warmer cells indicate more likely gas saturation values. The most likely saturation values are uniformly low across the profile: $0\% < S_g \leq 2\%$. Figure 5 also shows posterior distributions, but for total pressure. Again, the most likely values concentrate towards the lower end of the parameter range, around 0.6-1.2 MPa, largely falling within the lithostatic pressures at the top and bottom horizons (black lines in Figure 4). It is also possible to show the posterior distributions for the other 11 parameters in the simulator, but we choose to focus on these two more interesting parameters.

One important feature to note from Figures 4 and 5 is that there are no values in either sample space with absolutely zero probability density. This indicates that the Metropolis algorithm introduced sufficient mixing into the sampling of both parameters (and this holds true for the other 11 parameters too). Exploring the sample space is crucial for getting reliable posterior distributions, especially when the posteriors have multiple modes, as can occur with nonlinear simulators such as ours. In fact, some second modes are evident in the gas saturation posteriors (Figure 4), where clusters of isolated, higher density values appear at larger saturations. This corresponds to a property of this attenuation model observed in Morgan et al. (2012), where Q is bimodal with respect to gas saturation and the modes are typically at low and high saturation values.

Another feature of interest also relates to these diminutive second modes; the traces at which these are sampled most prominently are not spatially contiguous, but instead occur locally. For example, Trace 129 in Figure 4 has a strongly sampled second mode for saturation values ~80-100%, but none of its neighbors exhibits this. This behavior is a result of the Markov random field in our prior, which allows for occasional, isolated extreme values. Had we based our prior on, say, a Gaussian Markov random field, such local variability would have been diminished.

Discussion

The hierarchical modeling gives reasonable gas saturation posterior distributions. 0-2% agrees with saturation values for other sediments with gas bubble inclusions, which are typically less than 10% (Holbrook et al., 1996; Haacke et al., 2007). These values obtained here are slightly larger than the ~0.1% values obtained in Morgan et al. (2012). In terms of slope stability, the low gas saturation posterior estimates would allow one to assume fully saturated soil conditions. Just a few percent gas saturation will not change the bulk suction behavior of the soil, thus avoiding partially saturated analyses. The actual presence of this small amount of gas should have no deleterious effect on slope stability at this site.

The posterior distributions for pressure may be somewhat less reliable and useful than those for gas saturation, and remain a work in progress. First, the model for attenuation (simulator) is not as sensitive to pressure as it is to gas saturation, as well as porosity, permeability, and a few other parameters. This shows up in the posterior distributions (Figure 5), where the densities are more uniformly distributed against pressure (vertically in the image). To get a better picture of this, an example histogram of the posterior from Trace 160 is shown in Figure 6a. This histogram has a more dispersed form than the posterior for saturation from the same trace (Figure 6b). The greater dispersion indicates that the likelihood changes very little over a wide range of pressure values. The presence of a common, single mode around 0.7-1.0 MPa suggests some preference for these particular pressure values, but this comes with relatively great uncertainty because a broad range of pressure values have substantial probability densities too. The lack of sensitivity that the attenuation model has to pressure is perhaps due to the fact that the model is for P-wave attenuation, and P-waves are not sensitive to pore pressure. S-waves are, however, sensitive to pore pressures, and so a similar approach using an S-wave model and dataset may give better pressure estimates.

The large uncertainty in these pressure values makes this approach not as useful for slope-stability investigation. While the pressure values we obtain are generally reasonable, falling with the majority of likelihood within the lithostatic pressure limits of our layer, these results are not precise enough to yield reliable excess pore pressure estimates. If we subtract the average hydrostatic pressure in our layer from these pressure posterior distributions, we get posterior distributions for excess pore pressure (Figure 7). Here, we have a large range of likely excess pore pressures that has a mode at ~100 kPa. Excess pore pressures around 100 kPa intuitively seem too high for such a shallow setting. The top horizon in Figure 3a is about 55 m water depth and 7 m below seabed surface on average, and the bottom horizon is about 92 m water depth and 44 m below seabed surface on average. Using the initial values in Table 1 to get a bulk density of 1615 kg/m^3 , we can calculate the effective vertical stress at the top and bottom horizons as about 40 and 250 kPa. With 100 kPa excess pore pressure, this gives excess pore pressure ratios exceeding unity at the top and equal to 40% at the bottom. Obviously, such excess pore pressure ratios are too high, and this can be further witnessed when comparing to field data. In situ piezometer measurements of pore pressure taken nearby in the fjord give excess pore pressure ratios from 12 to 31% (Vanneste et al., 2013). The latest readings from these two piezometers, spanning from October 2012 to November 2013, give ratios around fluctuating around 11% for one site, and around 17% for the other.

Conclusion

Coupling the Bayesian hierarchical approach with the chosen attenuation model gives far more certain estimates of gas saturation than pore pressure. The better performance in inverting for gas saturation comes from the high sensitivity that the attenuation model has to this parameter. On the other hand, the model is not very sensitive to pressure. We still see an obvious mode in the pressure posterior distributions that falls within realistic lithostatic pressures, but the high dispersion of these distributions gives great uncertainty to any point estimates and yield unrealistic excess pore pressure values.

In this paper, we apply our results from the posteriors towards the problem of slope stability at Finneidfjord. We find that the gas saturations are not sufficient to significantly alter the matric suction of the soils there. The methodology developed in this paper would also be useful for natural gas reservoir characterization. Gas saturations in such environments are much larger than those observed at Finneidfjord, however we see in this paper that the Bayesian hierarchical inversion scheme is fully capable of exploring gas saturations greater than 70% with the attenuation model used here.

References

- Bünz, S., Mienert, J., Vanneste, M., and K. Andreassen, K. 2005. Gas hydrates at the Storegga Slide: Constraints from an analysis of multicomponent, wide-angle seismic data. *Geophysics* **70** (5): B19–B34.
- Carcione, J. M., and Picotti, S. 2006. P-wave seismic attenuation by slow-wave diffusion: Effects of inhomogeneous rock properties. *Geophysics* **71** (3): O1–O8.
- Dutta, N. C., and Sheriff, A.J. 1979. On White's model of attenuation in rocks with partial gas saturation. *Geophysics* **44**: 1806–1812.
- Ecker, C., Dvorkin, J., and Nur, A. M. 2000. Estimating the amount of gas hydrate and free gas from marine seismic data. *Geophysics* **65**: 565–573.
- Haacke, R. R., Westbrook, G. K., and Hyndman, R. D. 2007. Gas hydrate, fluid flow and free gas: Formation of the bottom-simulating reflector. *Earth and Planetary Science Letters* **261**: 407–420.
- Higdon, D., Reese, C.S., Moulton, J.D., Vrugt, J.A., and Fox, C. 2008. Posterior exploration for computationally intensive forward models. In: *Handbook of Markov Chain Monte Carlo*. Boca Raton, Florida: CRC Press.
- Holbrook, W. S., Hoskins, H., Wood, W. T., Stephen, R. A., and Lizarralde, D. 1996. Methane hydrate and free gas on the Blake Ridge from vertical seismic profiling. *Science* **273**: 1840–1843.
- Hou, Z., Rubin, Y., Hoversten, G.M., Vasco, D., and Chen, J. 2006. Reservoir-parameter identification using minimum relative entropy-based Bayesian inversion of seismic AVA and marine CSEM data. *Geophysics* **71** (6): O77-O88.
- Lee, M.W., and Collett, T.S. 2009. Unique problems associated with seismic analysis of partially gas-saturated unconsolidated sediments. *Marine and Petroleum Geophysics* **26**: 775–781.
- Mavko, G., Mukerji, T., and Dvorkin, J. 1998. *The rock physics handbook: Tools for seismic analysis in porous media*, second edition, 522. New York: Cambridge University Press.
- Morgan, E.C., Vanneste, M., Lecomte, I., Baise, L.G., Longva, O., and McAdoo, B. 2012. Estimation of free gas saturation from seismic reflection surveys by the genetic algorithm inversion of a P-wave attenuation model. *Geophysics* **77** (4): R175-R187.
- Reine, C., van der Baan, M., and Clark, R. 2009. The robustness of seismic attenuation measurements using fixed- and variable-window time-frequency transforms. *Geophysics* **74** (2): WA123–WA135.
- Schön, J., 1996. *Physical properties of rocks: Fundamentals and principles of petrophysics*, first edition, 600. New York: Pergamon.
- Stenerud, V., Kippe, V., Lie, K., and Datta-Gupta, A. 2008. Adaptive multiscale streamline simulation and inversion for high-resolution geomodels. *SPE J* **13** (1): 99-111.
- Vanneste, M., Longva, O., L'Heureux, J.S., Vardy, M.E., Morgan, E., Forsberg, C.F., Kvalstad, T.J., Strout, J.M., Brendryen, J., Haflidason, H., Lecomte, I., Steiner, A., Kopf, A., Morz, T., and Kreiter, S. 2013. Finneidfjord, a Field Laboratory for Integrated Submarine Slope Stability Assessments and Characterization of Landslide-Prone Sediments: A Review. Paper 13OTC-P-686-OTC presented at the Offshore Technology Conference 2013.
- Vardy, M.E., L'Heureux, J.S., Vanneste, M., Longva, O., Steiner, A., Forsberg, C.F., Haflidason, H., and Brendryen, J. 2012. Multidisciplinary investigation of a shallow near-shore landslide, Finneidfjord, Norway. *Near Surface Geophysics* **10**: 267-277.
- White, J. E. 1975. Computed seismic speeds and attenuation in rocks with partial gas saturation. *Geophysics* **40**: 224–232.
- Zillmer, M. 2006. A method for determining gas-hydrate or free-gas saturation of porous media from seismic measurements. *Geophysics* **71** (3): N21–N32.

Appendix: Model of P-wave Attenuation in Partially Saturated Marine Soils

The following specifies the system of equations used in the simulator presented in the “Theoretical Model” section. This appendix nearly reproduces the model introduced by Carcione and Picotti (2006), with some minor adjustment. We urge our audience to read Carcione and Picotti (2006) to more fully understand the features of this model. Because in situ methane behaves as a real gas, for a given gas pressure P (Pa) and temperature T (°C) above the critical temperature of -82.7°C, we can solve the van der Waals equation, $(P + A\rho_g^2)(1 - B\rho_g) = \rho_g R(T + 273)$ for gas density ρ_g (kg/m³). Here, $R = 519.4$ J/(kgK), $A = 879.9$ Pa(m³/kg)², and $B = 2.675 \times 10^{-3}$ m³/kg. Using this ρ_g , we can find the bulk modulus for gas:

$$K_g = \frac{4}{3} \left[\frac{\rho_g R(T + 273)}{(1 - B\rho_g)^2} - 2A\rho_g^2 \right]$$

For known porosity ϕ , solid grain bulk modulus K_S and solid grain shear modulus μ_S , the dry-rock bulk and shear moduli are

$$K_m = K_s(1 - \phi)^{\left\{ \frac{4}{(1-\phi)} \right\}}$$

and $\mu_m = K_m \mu_s / K_s$ respectively. The Gassmann modulus K_G is found as $K_G = K_m + \alpha^2 M$, where $\alpha = 1 - K_m / K_s$ and $M = K_s / (1 - \phi - K_m / K_s + \phi K_s / K_f)$. The bulk fluid modulus $K_f = K_w$ for the water-saturated sublayer and $K_f = K_g$ for the gas-saturated sublayer. Here we consider a system of layered porous media and denote the water-saturated sublayer with subscript 1 and the gas-saturated sublayer with 2. These sublayers have thicknesses d_1 and d_2 , respectively, and $d = d_1 + d_2$. Furthermore, $S_g = \frac{d_2}{d} * 100\%$. The complex bulk modulus is

$$E = \left[\frac{1}{E_0} + \frac{2(r_2 - r_1)^2}{i\omega(d_1 + d_2)(I_1 + I_2)} \right]^{-1},$$

where i is the imaginary unit, ω is angular frequency, and $E_0 = \left(\frac{p_1}{E_{G_1}} + \frac{p_2}{E_{G_2}} \right)^{-1}$ with $p_j = \frac{d_j}{d_1 + d_2}$ and $E_j = K_{G_j} + \frac{4}{3}\mu_m$ for $j = 1, 2$. Furthermore, omitting the subscript j for clarity, the ratio of fast P-wave fluid tension to total normal stress is $r = \alpha M / E_G$, and the impedance related to the slow P-wave is $I = \frac{\eta}{\kappa k} \coth(kd/2)$, where the slow P-wave complex number is $k = \sqrt{\frac{i\omega\eta}{\kappa K_E}}$, the effective modulus is $K_E = E_m M / E_G$ and the dry-rock fast P-wave modulus is $E_m = K_m + \frac{4}{3}\mu_m$.

With the average density $\bar{\rho} = p_1\rho_1 + p_2\rho_2$, and the complex velocity defined by $\bar{\rho} v^2 = E$, we get the loss angle $\theta = \tan^{-1}[\Im(v^2)/\Re(v^2)]$, with \Im and \Re giving the imaginary and real components, respectively. Finally, we obtain the quality factor via $Q^{-1} = \tan \theta$. Here, we evaluate these equations over the range of $\omega = 2\pi f$ given in the Methods section and take $Q(\theta)$ as the minimum resulting Q value over this frequency range.

Table 1. Initial parameter values and parameter bounds.

Parameter	Lower bound	Initial value	Upper bound
Gas saturation S_g (%)	0	0	100
Total pressure P (MPa)	~0.55	~0.55	~2.93
Porosity ϕ	0.64	0.65	0.66
Permeability κ (Darcy)	10^{-8} ^a	10^0	10^5 ^a
Solid grain bulk modulus K_s (GPa)	20 ^b	30	70 ^b
Solid grain shear modulus μ_s (GPa)	5 ^b	13	50 ^b
Solid grain density ρ_s (g/cc)	2.55 ^b	2.65	2.71 ^b
Water bulk modulus K_w (GPa)	2.00	2.25 ^c	2.50
Water density ρ_w (g/cc)	1.000	1.025	1.030
Water viscosity η_w (Pa·s)	0.001	0.003 ^c	0.005
Gas viscosity η_g (10^{-4} Pa·s)	1.0	1.5 ^c	2.0
Temperature T (°C)	0	5	10
Layer thickness d (m)	36.5	37.5	38.5

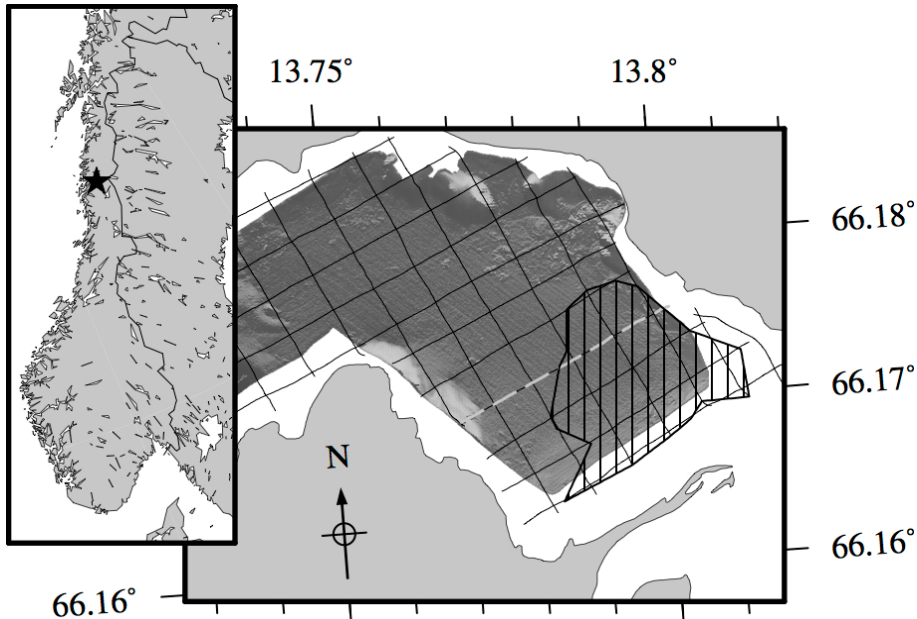
^a Schon (1996)^b Mavko (1998)^c Carcione and Picotti (2006)

Figure 1. Location map of Finneidfjord, Norway (starred in left panel). The right panel shows the orientation of airgun seismic survey lines over bathymetry of the fjord. The gray dashed line is Line08, containing the profile data used in this paper. The black hatched polygon maps the extent of a subseabed free gas deposit.

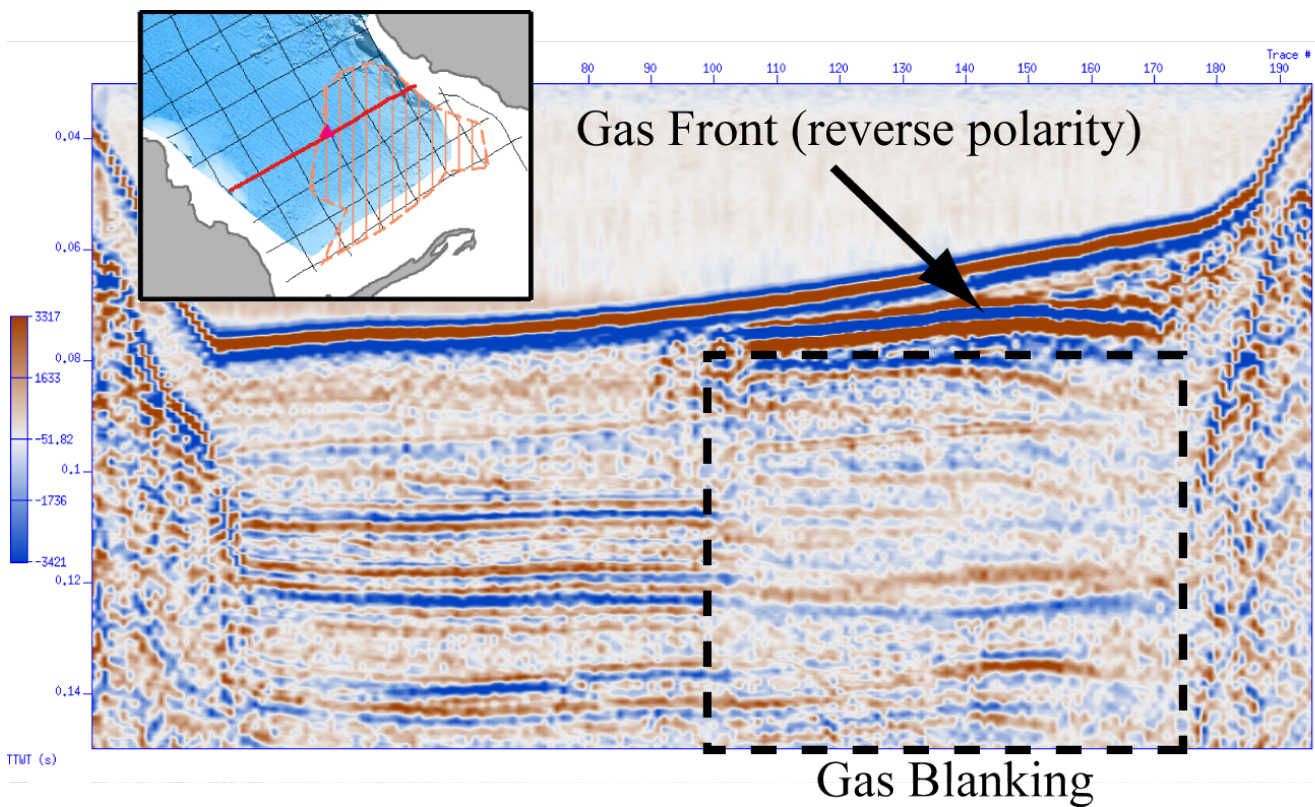


Figure 2. Image of seismic reflection profile at Line08. It is inferred that free gas in the sediment to the right of the profile is creating the strong amplitude, reverse polarity reflection, as well as the muted signal (gas blanking) beneath this.

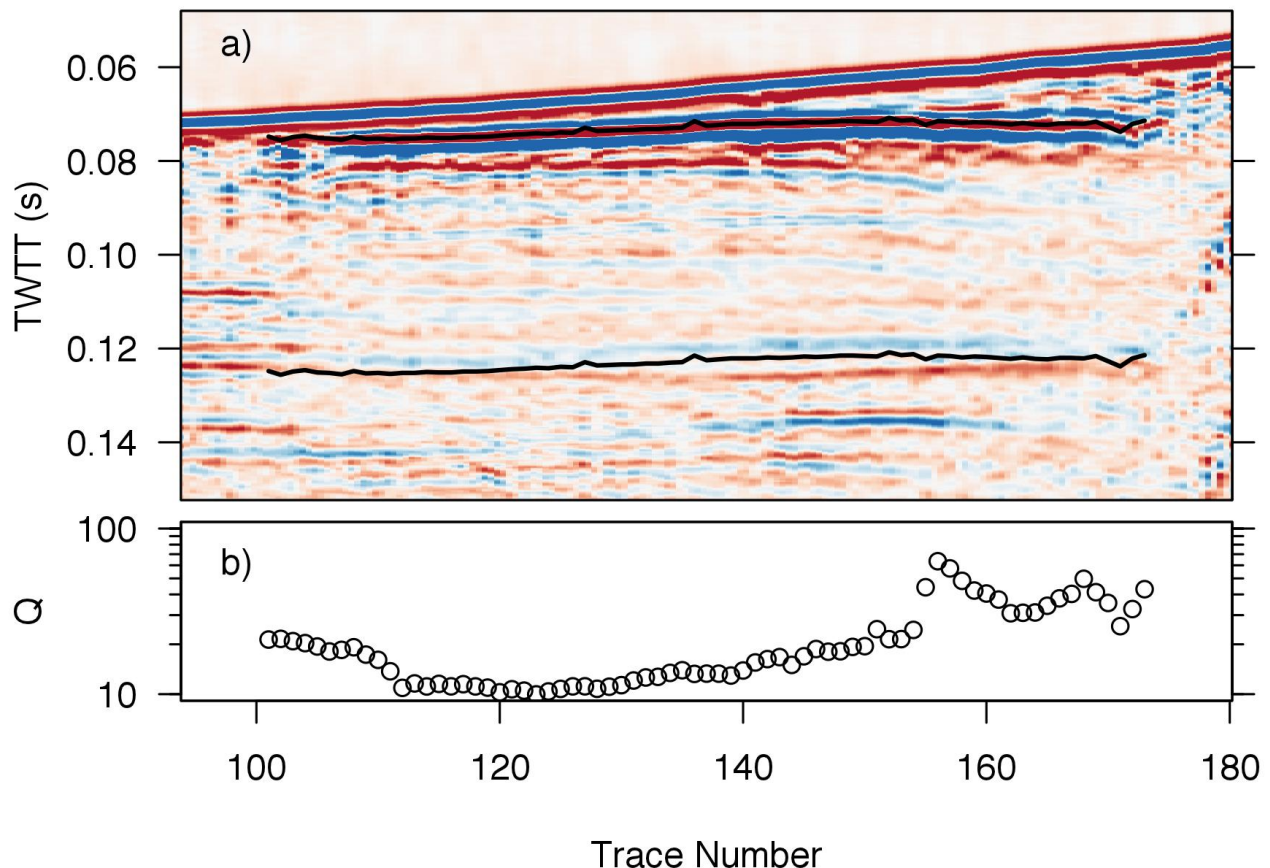


Figure 3. The seismic reflection data with the chosen horizons (a) and resulting quality factor (Q) measurements (b; note the log scale).

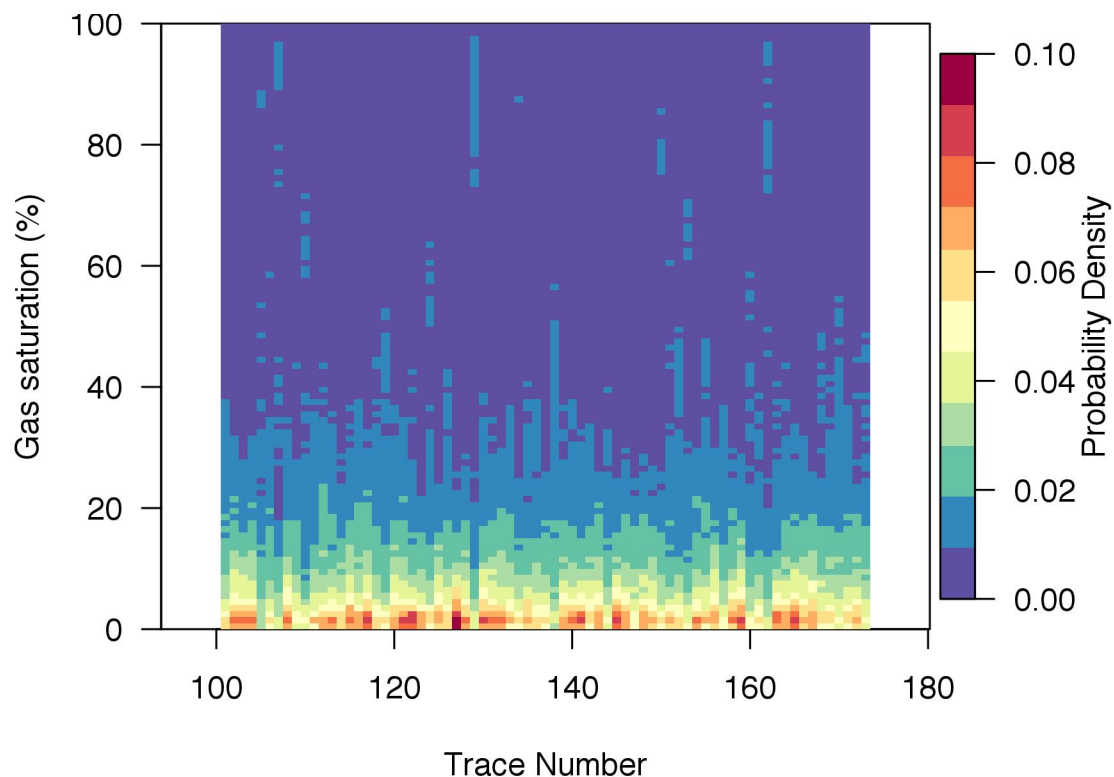


Figure 4. Gas saturation posterior probability densities for each trace in the analysis.

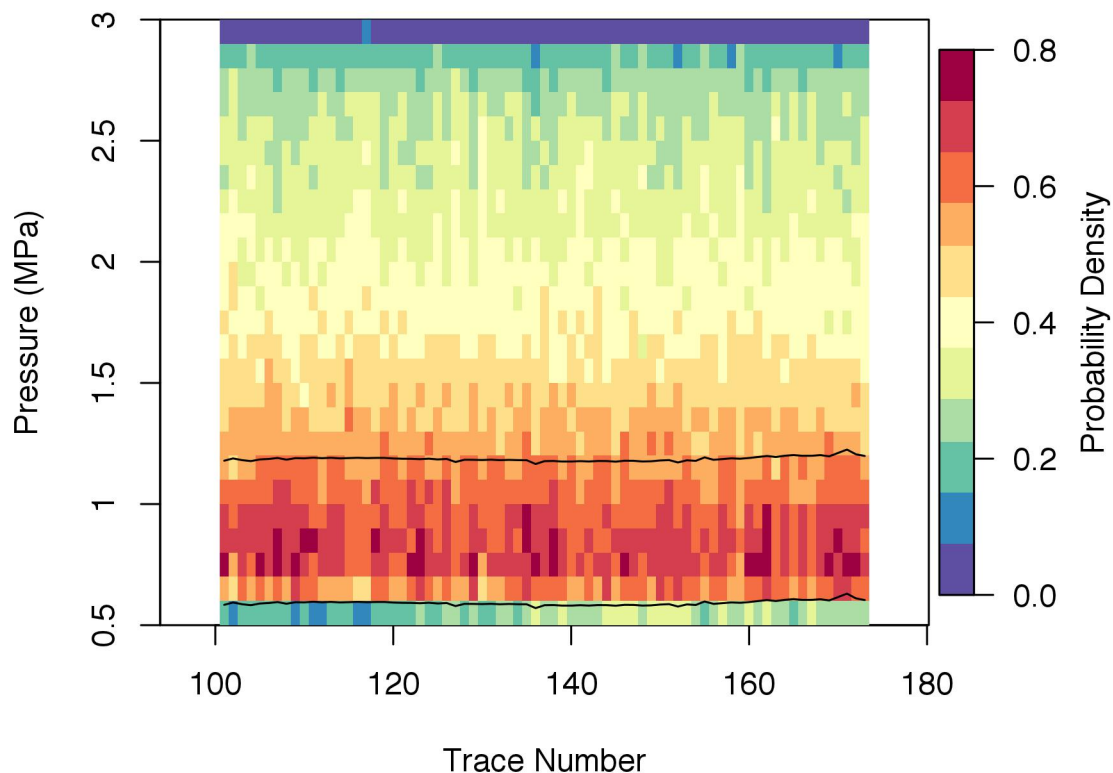


Figure 5. Total pressure posterior probability densities for each trace in the analysis. The two horizontal black lines represent the lithostatic pressures at the top horizon (lower line) and bottom horizon (upper line).

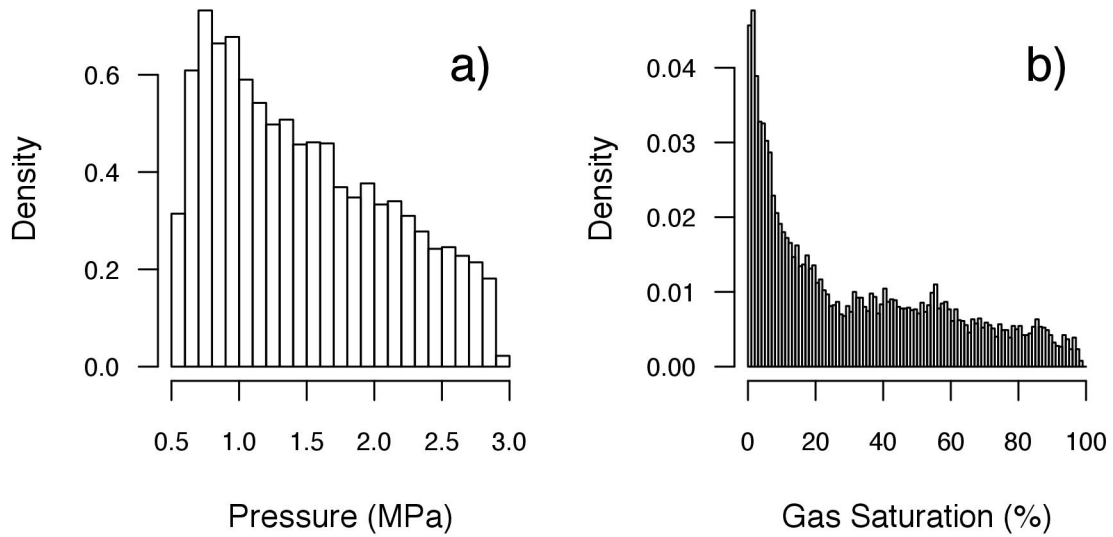


Figure 6. Histograms of posterior samples from Trace 160 for excess pore pressure (a) and gas saturation (b).

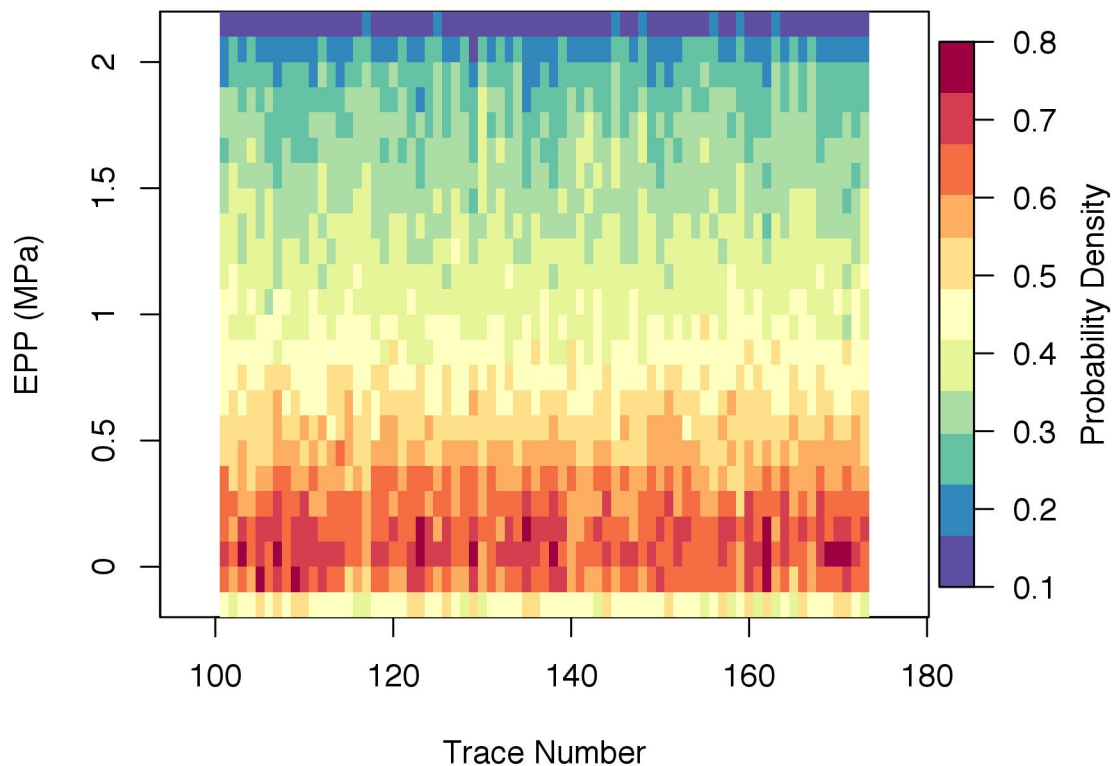


Figure 7. Excess pore pressure posterior probability densities for each trace in the analysis.